SI Methods

Protein expression and purification

Unless stated, a 20 mM ammonium acetate buffer at pH 7.0 was used and referred to here as final buffer. Tau, RNA, NaCl, PEG and other stocks were prepared using final buffer. Measurements were taken in final buffer at room temperature unless stated.

N-terminal truncated, microtubule binding domain containing tau187 (residues 255-441 with a His-tag at the N-terminus) were used for *in vitro* studies. The clonning, expression, and purification have been previously described [1], [2]. The single cysteine variant of tau187 (tau187C291S) were generated via site-direct mutagenesis. E. coli BL21 (DE3) cells previously transfected were cultured from frozen glycerol stock overnight in 10 mL luria broth (LB) which was used to inoculate 1 L of fresh LB. Culturing and inoculation were performed at 37 °C with shaking of 200 rpm. At OD_{600} of 0.6–0.8, tau187 variant expression was induced by incubation with 1 mM isopropylß-D-thiogalactoside (Sigma Aldrich) for 2–3 h. Cells were harvested by centrifugation for 30 min at 5000 × g (Beckman J-10; Beckman Instruments, Inc.), and the pellets were stored at −20 °C until further use.

Cell pellets were resuspended in lysis buffer (Tris-HCl pH 7.4, 100 mM NaCl, 0.5 mM DTT, 0.1 mM EDTA, 1mM PMSF) with 1 Pierce protease inhibitor tablet (Thermo Fisher). Lysis was initiated by the addition of lysozyme (2 mg/ml), DNase (20 µg/ml), and $MgCl_2$ (10 mM) and incubated for 30 min on ice. Lysate was then heated to 65 °C for 13 min, cooled on ice for 20 min and then centrifuged to remove the precipitant. The supernatant was loaded onto a Ni-NTA agarose column pre-equilibrated with wash buffer A (20 mM sodium phosphate pH 7.0, 500 mM NaCl, 10 mM imidazole, 100 µM EDTA). The column was then washed with 20 ml of buffer A, 15 ml buffer B (20 mM sodium phosphate pH 7.0, 1 M NaCl, 20 mM imidazole, 0.5 mM DTT, 100 µM EDTA). Purified tau187 was eluted with buffer C (20 mM sodium phosphate pH 7.0, 0.5 mM DTT, 100 mM NaCl) supplemented with varying amounts of imidazole increasing from 100 mM to 300 mM. The protein was then concentrated via centrifugal filters (MWCO 10 kDa; Millipore Sigma) and the buffer was exchanged into final buffer by PD-10 desalting column (GE Healthcare). The final protein concentration was determined by UV-Vis absorption at 274 nm using an extinction coefficient of 2.8 $cm^{-1}mM^{-1}$, calculated from absorption of Tyrosine [3].

Spin labeling and cw EPR

Freshly eluted tau187C291S (with one cysteine at site 322) was replaced in final buffer using a PD-10 desalting column (GE Healthcare). Protein after PD-10 was labeled overnight at 4°C by immediately mixing with a 10-fold molar excess of the spin label (1-oxyl-2,2,5,5-tetramethylpyrroline-3-methyl)

methanethiosulfonate (MTSL; Toronto Research Chemicals), resulting in spin labelled tau (tau187C291S-SL). Excess label was removed using PD-10. The protein was concentrated using centrifugal filter (MWCO 10 kDa; Amicon) and the final protein concentration was determined by UV-Vis absorption at 274 nm as mentioned above. Non-labeled tau187C291S was used in order to achieve spin dilution.

Cw EPR measurements were carried out using a X-band spectrometer operating at 9.8 GHz (EMX; Bruker Biospin, Billerica, MA) and a dielectric cavity (ER 4123D; Bruker Biospin, Billerica, MA). 100 μM tau187C291S-SL was mixed with 400 μM tau187C291S to reach 20% spin labeling. Samples under droplet forming condition were prepared by adding 1.5 mg/ml RNA, and tau samples under aggregation-inducing conditions prepared by adding 125 μM heparin (15 kDa average MW; Sigma-Aldrich). A sample of 4.0 μl volume was loaded into a quartz capillary (CV6084; VitroCom) and sealed at both ends with critoseal, and then placed in the dielectric cavity for measurements. Cw EPR spectra were acquired by using 6 mW of microwave power, 0.5 gauss modulation amplitude, 100 gauss sweep width, and 8-64 scans for signal averaging.

Cw EPR spectra analysis

The recorded cw EPR spectra were subjected to single- or double-component simulation. EPR simulation and fitting were performed using MultiComponent, a program developed by Christian Altenbach (University of California, Los Angeles). For all spectra fitting, the magnetic tensors A and g were fixed and used as constraints as previously reported [3]. These values are A_{xx} = 6.2 G, A_{yy} = 5.9 G, A_{zz} = 37.0 G, and g_{xx} = 2.0078, g_{yy} = 2.0058, and g_{zz} = 2.0022.

For soluble tau, the cw EPR spectra were best fitted with a single-component simulation and the rotational diffusion constant (R) can be extracted. The rotation correlation time τ_R was calculated using $\tau_R = 1/(6R)$. For tau-heparin aggregates, the cw EPR were subjected to double-component simulation, where the parameters of the fitted single-component were used as a mobile-component. The immobile-component were set to be identical to the mobile-component, except the diffusion tensor tilt angle β_D = 36° and the order parameter S. The fitting parameters were limited at a minimum, which includes the population, p, rotational diffusion constants of mobile- and immobile-component, R_1 and R_2, and the order paramter, S of the immobile-component. The fitted immobile-component were used to represent the rotational correlation time for tau-heparin fibrils. For tau-RNA CC. the cw EPR spectra were subjected to both single- and double-component fitting. Comparing the two fitting schemes showed that singl-component fitting has almost overlapped the cw EPR spectra, while double-component fitting results in a immobile-component population of ~10% (data not shown). This showed that tau-RNA CC cw EPR spectra can be sufficiently fit with single-component. The fitted rotational correlation time was calculated and plotted against tau-heparin samples.

Turbidimetry and brightfield microscopy

Turbidity of samples at room temperature were represented by optical density at a 500-nm wavelength (OD_{500}), using a Shimadzu UV-1601 spectrophotometer (Shimadzu Inc.). The amount of coacervates in a sample were approximated to be propotional to its OD_{500}.

Tubidity of samples at ramping temperatures were represented by OD_{500} measured using Jasco J-1500 CD Spectrometer (JASCO Inc.) equipped with temperature controller and spectrophotometer. 120 µL of 20 µM tau187C291S, 60 µg/mL polyU RNA and 30 mM NaCl in working buffer were prepared in a 100 µL cuvette (Starna Scientific Ltd) and kept at 4 °C for 5 min before cycling. Heating and cooling temperatures were ramped at 1 °C/min while OD_{500} was monitored.

Bright field images were examed to confirm the presence of tau-RNA CC. 100 µM tau187C291S and 300 µg/mL polyU RNA was mixed in presence of 20 mM ammonium acetate and 30 mM NaCl. 10 µl of the mixture was pipetted onto a microscope slide with a cover slide gapped by two layers of double-sided sticky tape. Temperatures were controlled using an incubator. Bright field images were acquired using a spectral confocal microscope (Olympus Fluoview 1000; Olympus, Center Valley, PA).

Determining tau-RNA CC composition

It was shown by fluorescence microscopy in protein-RNA LLPS that protein is concentrated inside the droplet [4, p. 1], [5]. For representing tau inside the droplets with measurement taken from droplet suspension, we quantified the percentage of tau present as droplets. After mixing and centrifuging 60 µL droplet suspension of 400 µM tau187/322C and 1500 µg/mL polyU, ~1 µL dense phase was generated with clear boundary against dilute phase. Dissolving dense phase in high concentration of NaCl resulted in transparent solution thus UV absorption can be measured.

Due to the difficulty of preparing large volume of pure dense phase, we can only underestimate the tau and polyU concentration in dense phase. Since tau and RNA have different UV absorbance spectra, fitting spectra of the tau-RNA mixed sample with those of pure tau and polyU generated the concentration of both. Fitting results showed that over 99% of the tau and over 99.9% of polyU were condensed inside the dense phase. This partitioning guaranteed that the property of tau in the droplet suspension represents those in the droplets.

Cell Culture and confocal microscopy

Protein (tau187 or K18) was labeled with Alexa Fluor® 488 or 555 5-SDP ester (Life Technologies) according to the suppliers instructions. After labeling, 100 mM glycine was added to quench the reaction and the proteins were subjected to Zeba desalting columns (Thermo Scientific) to remove any unreacted

label. Average label incorporation was between 1 and 1.5 moles/mole of protein, as determined by measuring fluorescence and protein concentration (A_{max} × MW of protein / [protein] × ε_{dye}).

H4 neuroglioma cells (ATCC® HTB-148) were cultured in DMEM supplemented with 10% FBS, 100 µg/ml penicillin/streptomycin. Cultures were maintained in a humidified atmosphere of 5% CO_2 at 37°C. Tau protein (1:20 labeled K18:unlabeled tau114), RNA, PEG, and media (DMEM,10% FBS,1% Pen/Strep) were mixed at the indicated concentrations and added to cells at varying temperatures. Images were obtained on a Leica SP8 Resonant Scanning Confocal.

Flory-Huggins based Voorn-Overbeek (FH-VO) modeling

FH-VO is based on a Flory-Huggins (FH) treatment, where the polymer system is mapped onto a lattice. Voorn and Overbeek extended the FH formalism to polyelectrolytes by including long-ranged electrostatic interactions with a Debye–Hückel term. The resulting expression for the free energy of mixing (ΔGmix) per lattice site is

$$\frac{\Delta G_m}{M k_B T} = \sum \frac{\phi_i}{N_i} ln\phi_i - \alpha[\sum \sigma_i \phi_i]^{\frac{3}{2}} + \sum \chi_{ij} \phi_i \phi_j \qquad \text{(S1)}$$

Where $M = V/(l_w)^3$ is the total number of lattice sites. In Eqn.S1, the index *i* refers to one of the five species. N_i is the degree of polymerization for species *i*. For tau187 and tau114, N_i equals to the length of the polypeptides (Table S1); while for RNA, N_i is estimated by the average MW 900 kDa for polyU RNA and the MW of condensated uridine monophosphate, 306 Da. For monovalent ions and water, $N_i = 1$.

σ_i is the average charge per monomer, which is determined by (net charge) / N_i. The net charges of tau at experimental pH conditions (pH = 7) were estimated based on primary sequences in Table S1, using pepcalc.com. σ_i for other species were listed in Table S2. In FH-VO model, σ_i is fixed. We also consider a modified version, a FH-VO-CR model, where σ_i of RNA is set to a function of temperature as discussed further below.

In Eqn. S1, ϕ_i is the volume fraction of species (tau, RNA, Na^+, Cl^-, H_2O). ϕ_i was computed by $\phi_i = c_i \times N_i \times \frac{1}{c_w}$ where c_i is the molar concentration and c_w the molar concentration of pure water computed from water volume molarity: $c_w = 55.56$ mol/L. In experiments, c_{tau} and c_{RNA} were designed to reach a 1:1 charge ratio, therefore, we have $N_{RNA} \times c_{RNA} = 11 \times c_{tau} = 11 \times [\text{tau}]$. In addition to NaCl, there is 20 mM ammonium acetate in the buffer. The total monovalent salt concentration is $c_{salt} = c_{NaCl} + 20\,mM = [NaCl] + 20\,mM$. Therefore, ϕ_i were calculated from experimental [tau] and [NaCl] as,

$$\phi_{tau} = [tau]\times 207\times \frac{1}{c_w}$$
$$\phi_{RNA} = [tau]\times 11\times \frac{1}{c_w}$$
$$\phi_{salt} = ([NaCl] + 20\ mM)\times \frac{1}{c_w} \quad \text{(S2)}$$
$$\phi_{polymer} = \phi_{tau} + \phi_{RNA} = [tau]\times 218\times \frac{1}{c_w}$$
$$\phi_{water} = 1 - \phi_{polymer} - \phi_{salt}$$

α is the strength of the electrostatic interactions defined as

$$\alpha = \frac{2}{3}\sqrt{\frac{\pi}{l_w^3}}\left(\frac{e^2}{4\pi\epsilon_r\epsilon_0 k_B T}\right)^{3/2} \quad \text{(S3)}$$

where l_w is the length of a lattice, computed from c_w, $l_w = \sqrt[3]{\frac{1\times10^{-3}m^3}{c_w N_A}}$, $\epsilon_r\epsilon_0$ the water permitivity, $\epsilon_r\epsilon_0 = 80\times8.85\times10^{-12}\ F/m$, k_B the Boltzmann constant and T the absolute temperature.

χ_{ij} is the Flory-Huggins interaction parameter between species i and j, which will be defined and descussed below.

The three terms on the right-hand side of Eqn. S1 are respectively: 1) the ideal Flory-Huggins mixing entropy, 2) the mixing enthalpy due to Coulombic interactions based on Debye–Hückel approximation [6] and 3) the excess free energy to account for the non-Coulombic interactions, which can include contributions from water perturbation [7], cation-π interaction [8] and dipole-dipole interactions [9]. Eqn. S1 has been successfully applied in PDMAEMA-PAA complex coacervate [10]. In this work we refer to Eqn. S1 as FH-VO model, which is a minimal model for complex coacervation.

Determining phase separation temperature

A phase separation temperature, T_{cp}, was assigned to the cloud point of the sample. T_{cp} was determined by fitting normalized turbidity-temperature curves to a sigmoid function as follows

$$normalized\ turbidity = \frac{1}{1 + exp\left(-k\times\left(T - T_{cp}\right)\right)},$$

to find

$$T = T_{cp}.$$

FH-VO bindal curve computation

ϕ_i and T can be converted from/to experimental conditions as described, where tau and RNA are added at a fixed charge neutrality ratio. Therefore, ΔG_{mix} depends on four variables: total polymer volume fraction $\phi_{polymer} = \phi_p + \phi_q$, total salt volume fraction $\phi_{salt} = \phi_{s+} + \phi_{s-}$, temperature T and X, a matrix of $\chi_{pp}, \chi_{pq}, \chi_{ps+}, \dots, \chi_{qp}, \chi_{qq}, \dots$. A two-phase equilibrium exists where the sum of mixing free energy of two coexisting phases are lower than that of the homogeneous mixture. For simplicity, we adopt the assumption that the salt concentration in both two phases are identical [10], leaving the system a binary mixture of polymer and buffer. Binodal compositions are defined by pairs of points on the curve of ΔG_{mixing} vs. $\phi_{polymer}$ that have common tangents, corresponding to compositions of equal chemical potentials of both buffer and polymer in dense and dilute phases.

A binodal composition curve (binodal curve) was computed by finding the bi-tangent points of ΔG_{mixing} vs. $\phi_{polymer}$ at a series of ϕ_{salt} at given temperature T and given parameters. Given ϕ_{salt}, T and X, the mixing free energy is solely dependent on $\phi = \phi_{polymer}$:

$$f(\phi) = \Delta G_{mixing}(\phi_{polymer})$$

A bi-tangent pair (ϕ_1, f_1), (ϕ_2, f_2) was calculated by solving the set of nonlinear equations [11], [12],

$$\begin{cases} \left.\dfrac{\partial f}{\partial \phi}\right|_{\phi=\phi_1} - \left.\dfrac{\partial f}{\partial \phi}\right|_{\phi=\phi_2} = 0 \\ \left.\left(f - \phi\dfrac{\partial f}{\partial \phi}\right)\right|_{\phi=\phi_1} - \left.\left(f - \phi\dfrac{\partial f}{\partial \phi}\right)\right|_{\phi=\phi_2} = 0 \end{cases}$$

which was solved by R function *nleqslv* using Newton-Ralphson algorithm at given initial guess. Finally, the $\phi_{polymer}$ and ϕ_{salt} were converted into [tau] and [NaCl] as described.

Coarse grained polyelectrolyte model used in FTS

Our system consists of n total polymers made up of n_τ tau molecules of length N_τ and n_p RNA molecules of length N_p. Each amino acid is treated as a single Kuhn segment of length b. The solvent is treated implicitly with a uniform dielectric background ϵ. For simplicity we only consider the symmetric case of $N_p = N_\tau$. Chain connectivity is enforced by a harmonic bond potential of the form $\beta U_{bond} = \frac{3}{2b^2}\sum_{\alpha=1}^{n}\sum_{j=1}^{N}(|\boldsymbol{r}_{\alpha,j} - \boldsymbol{r}_{\alpha,j-1}|)^2$ where $\boldsymbol{r}_{\alpha,j}$ is the coordinates of bead j on chain α. In addition to chain connectivity, all monomers interact with a short-ranged excluded volume potential [13]. We take the well-

known Edward's delta function model for the excluded volume interaction $\beta U_{ex} = v\delta(\boldsymbol{r})$ where v is the excluded volume parameter [13]. The charge of each bead j for the tau molecule $z_{\tau,j}$ is determined from the primary amino acid sequence with aspartic (D) and glutamic (E) acid being $z_{\tau,j} = -1$, arginine (R) and lysine (K) being $z_{\tau,j} = +1$ and all other amino acids being neutral $z_{\tau,j} = 0$. The RNA chain is treated as a fully-charged chain with $z_{p,j} = -1$ for all monomers. Charged segments interact via a long-ranged Coulomb potential $\beta U_{el} = \frac{l_B z_i z_j}{r}$ with $l_B = \frac{e^2}{4\pi\epsilon_0\epsilon_r k_B T}$ being the Bjerrum length, e is the unit of electronic charge, ϵ_0 is the vacuum permittivity, and ϵ_r is the dielectric constant. For a schematic depiction of the polymer physics model see Fig 3 in the main text.

The model is ``regularized" by smearing all statistical segments over a finite volume instead of treating them as point particles [14]. This is accomplished by endowing each bead with a Gaussian profile with a width on the order of the statistical segment length $\Gamma(r) = (3/\pi b^2)^2 \exp(-3r^2/b^2)$ where r is a radial distance from the monomer center. As a consequence of this density smearing, the interactions between monomers ``softens" [15].

Transformation of particle model to a statistical field theory

The advantage of the coarse-grained polyelectrolyte model employed in this work is that it can be exactly converted to a statistical field theory by utilizing a Hubbard-Stratonovich transformation as described in [16]. Invoking this transformation, the canonical partition function is expressed in terms of two fluctuating auxiliary fields w and φ which serve to decouple the excluded volume and Coulombic interactions respectively [14], [16]–[19]. In the statistical field representations the canonical partition function is

$$Z = Z_0 \int Dw \int D\varphi \exp(-H[w,\varphi]) \qquad \text{(S4)}$$

where Z_0 contains the ideal gas partition function and self-interaction terms. The field-theoretic Hamiltonian for this model is

$$H[w,\varphi] = \frac{1}{2v}\int d\boldsymbol{r}\, w(\boldsymbol{r})^2 + \frac{1}{8\pi l_B}\int d\boldsymbol{r}\, |\nabla\varphi|^2 - n_\tau \ln\, Q_\tau[w,\varphi] - n_p \ln\, Q_p[w,\varphi] \quad \text{(S5)}$$

where $Q_\tau[w,\varphi]$ and $Q_p[w,\varphi]$ are the partition functions for a single tau and a single RNA molecule in the conjugate fields. These single chain partition functions can be computed using a Gaussian chain propagator such that

$$Q_l[\psi] = \frac{1}{V}\int d\boldsymbol{r}\, q_l(\boldsymbol{r}, N_l; \psi) \quad \text{(S6)}$$

where l indexes the chain type (tau/RNA) and $\psi(j) = i\,\Gamma \star \left(w + z_j\varphi\right)$ with $i = \sqrt{-1}$ and $\star$ a spatial convolution. The chain propagator $q_l(\boldsymbol{r}, j; \psi)$ is constructed from a Chapman-Kolmogorov-type equation

$$q_l(\boldsymbol{r}, j+1; \psi) = \left(\frac{3}{2\pi b^2}\right)^{3/2} \exp\left[-\psi(\boldsymbol{r}, j+1)\right] \int d\boldsymbol{r}' q_l(\boldsymbol{r}', j; \psi) exp\left(-\frac{3|\boldsymbol{r}-\boldsymbol{r}'|^2}{2b^2}\right) \quad \text{(S7)}$$

with initial condition $q_l(\boldsymbol{r}, 0; \psi) = \exp\left[-\psi(\boldsymbol{r}, 0)\right]$. From the field theoretic Hamiltonian any thermodynamic observable may be computed as an ensemble average of a corresponding operator expressed in terms of the field configurations $\tilde{G}[w, \varphi]$

$$\langle G \rangle = \frac{Z_0}{Z} \int Dw \int D\varphi\, \tilde{G}[w, \varphi] \exp\left(-H[w, \varphi]\right) \quad \text{(S8)}$$

We stress that no additional approximations are made in moving from a particle-based model to a statistical field theory. The advantage of such a transformation is that the pairwise interactions between monomers are decoupled in favor of interactions between monomers and a complex-valued field. This transformation is particularly suited to our purposes here as conventional particle simulations can only study the earliest stages of protein aggregation.

Field theoretic simulations using CL sampling

Field theoretic simulation (FTS) allows one to numerically compute ensemble averages of the form of Equation S8 by sampling along a stationary stochastic trajectory in the space of the field variables. The method has been presented in detail elsewhere [14], [16], [17]. We use complex Langevin (CL) sampling [18], [19] to stochastically sample the auxiliary fields. The method involves promoting the fields to be complex-valued and numerically propagating the CL equations of motion

$$\begin{aligned} \frac{\partial w(\boldsymbol{r},t)}{\partial t} &= -\lambda_w \frac{\delta H[w,\varphi]}{\delta w(\boldsymbol{r},t)} + \eta_w(\boldsymbol{r}, t) \\ \frac{\partial \varphi(\boldsymbol{r},t)}{\partial t} &= -\lambda_\varphi \frac{\delta H[w,\varphi]}{\delta \varphi(\boldsymbol{r},t)} + \eta_\varphi(\boldsymbol{r}, t) \end{aligned} \quad \text{(S9)}$$

where $\eta_w(\boldsymbol{r}, t)$ and $\eta_\varphi(\boldsymbol{r}, t)$ are real-valued Gaussian white-noise random variables with zero mean and variance proportional to the dissipative coefficients λ_w and λ_φ. A single FTS step involves computing the single chain partition functions for a given field configurations (w, φ) given by Equation S6 along with any operators $\tilde{G}[w, \varphi]$ followed by updating the field configurations according to Equation S9. Under the condition that the system is ergotic, ensemble averages are computed as time averages over the CL trajectory. All FTS-CL simulations were performed in reduced units by scaling spatial lengths by a reference distance $R_0 = b/\sqrt{6}$ corresponding to the prefactor in the scaling relation of an ideal

homopolymer radius of gyration with respect to the chain length $R_g = R_0 N^{1/2}$ [20]. Simulations were performed in a cubic box of length $L = 34.0\ R_0$ using periodic boundary conditions. Fields were sampled with a spatial collocation mesh of 32^3 sites. An exponential time difference (ETD) algorithm [21], [22] with $\Delta t = 0.01$ was used to numerically propagate the CL equations of motion Equation S13. All simulations were performed on NVIDIA Tesla M2070 or K80 graphics processing units (GPUs).

The thermodynamic state of the system is fully determined by specifying a dimensionless excluded volume parameter $B = v/{R_0}^3$, a dimensionless Bjerrum length $E = 4\pi l_B/R_0$, and a dimensionless polymer chain number density $C = \rho R_0^3$ with $\rho = \sum_l n_l N_l /V$ where l indexes the chain type (tau or RNA). Additionally, we require the fraction of chains of each type $\phi_l = n_l N_l / \sum_l n_l N_l$. In this work we consider only a 1:1 charge ratio, which for the model shown in Fig 1 corresponds to $\phi_\tau = 0.954$ and $\phi_p = 0.046$.

Determination of phase equilibria from FTS

In order to compute the phase coexistence points from FTS we need to compute the chemical potential μ and the osmotic pressure Π. The chemical potential operator for chain type l is $\widetilde{\mu_l} = \ln \frac{\rho {R_0}^3 \overline{\phi_l}}{N_l} - \ln Q_l$. For the pressure operator we use the form given in Appendix B of [23]. The conditions for the stable coexistence of two phases is given by the chemical equilibrium condition $\sum_l \nu_l {\mu_l}^I = \sum_l \nu_l {\mu_l}^{II}$ and the mechanical equilibrium condition $\Pi^I = \Pi^{II}$. The stoichiometric coefficient ν_l ensures charge neutrality. The procedure we employ in this work is that of [23], and involves computing the chemical potential and pressure for a range of polymer concentrations. Fig. S10 (Left) shows a plot of the osmotic pressure vs. the chemical potential for different polymer conentrations. The simulation data represent three branches: a dilute branch (red), a conentrated branch (blue), and an unstable branch (orange). The equilibrium condition of equal chemical potential and equal osmotic pressure can be directly gleaned from the intersection of the dilute and concentrated branch. This gives the critical conditions for phase coexistence. Fig. S10 (Right) show a plot of the chemical potential vs. polymer concentration. The critical chemical potential value is shown by the dashed horizontal line. The intersection of this line with the polymer concentration data points from FTS gives the dilute supernatant polymer concetration ρ^I and the coacervate concentration of the coexisting phase ρ^{II}. By repeating this procedure for many different thermodynamic conditions we can construct the phase diagrams shown in Fig. 5 of the main text.

Calculation of non-ionic entropy and enthalpy of coacervation

As discussed in the main text the interaction parameter is decomposed into an entropic and enthalpic contribution $\chi = \epsilon_s + \epsilon_H/T$. According to the Flory-Huggins treatment the non-combinatoric contribution to the Gibbs free energy of mixing is

$$\Delta G_{mix} = \mathrm{RTn}_p \chi \phi_w$$

where R is the ideal gas constant, T is the temperature, n_p is the total number of moles of monomer units, and ϕ_w is the volume fraction of water. From the relation $\Delta S_{mix} = -\frac{\partial \Delta G_{mix}}{\partial T}$, the non-ideal entropy of mixing is

$$\Delta S_{mix} = -\mathrm{Rn}_p \phi_w \epsilon_s.$$

From the relation $\Delta H_{mix} = \Delta G_{mix} + T\Delta S_{mix}$, the enthalpy of mixing arising from non-ionic interactions is

$$\Delta H_{mix} = \mathrm{Rn}_p \phi_w \epsilon_H.$$

Values in the main text are computed using a water volume fraction of $\phi_w = 0.722$. See Table S3 for further details.

SI Discussion:

The Effects of RNase in tau-RNA CC

The maximum turbidity of the samples was observed to steadily decrease over multiple cycles of heating and cooling. We suggested the decrease of maximum turbidity was due to degradation of RNA by ambient RNase. The observation that addition of RNase or RNase inhibitor respectively promotes or inhibits the decay of maximum turbidity of tau187-RNA CC supports this hypothesis (Fig S2).

Heparin induced amyloid fibrilization in tau-RNA CC

Although tau-RNA CC is at equilibrium, this does not imply subequent fibrillization could not be facilitated in the CC state when driving forces favoring tau aggregation are present or brought into the CC system. To answer whether tau retains its fibrillization capability, we prepared tau-RNA CC and subsequently doped this system with heparin to quantify the effectiveness of amyloid fibril formation. Tau-RNA CC was prepared with 100 μM tau187C291S-SL and 300 μg/mL polyA RNA in neutral buffer of 20 mM ammonium acetate in the presence of 19 vol % glycerol. Bright field images were taken after

10 minutes, showing an abundance of tau-RNA CCs (Fig S12 A). A replicate of the sample was prepared with additional 10 μM Thioflavin T and was incubated in room temperature for over 13 hours. The ThT fluorescence was recorded showing no sign of increase (Fig S12 C, black curve), indicating absence of amyloid fibrils, which is consistent with the equilibrium state of tau-RNA CC.

In parallel, a new sample of tau-RNA CC was prepared. After 10 minute of incubation, 25 μM of heparin (11 wt % of the total tau-RNA) was added and bright field images taken. Immediately after heparin addition, the tau-RNA CC phase vanished according to the bright field images and the solution appeared homogeneous (Fig S12 B), indicating the disassembly of tau-RNC CC. A replicate of the sample was monitored with 10 μM ThT added, and the fluorescence intensity compared to the sample without heparin addition. After heparin addition, the ThT fluorescence of the tau-RNA CC system increased significantly, demonstrating that tau is driven towards amyloid fibrillization (Fig S12 C, red curve). These observations suggest that while tau-RNA CC is principally and initially at equilibrium, that this system can be driven out of equilibrium upon adding factors that facilittate aggregation. The difference between tau-RNA vs tau-heparin interaction is likely that the former relies on weaker amine-carboxylate compared to the latter that engages in strong amine-sulfate associations, and so facilitates tau templating and tau-tau associations.

Non-ionic interactions were required in describing tau-RNA CC

To investigate the traditional Voorn-Overbeek model in describing tau-RNA CC, we first applied FH-VO model with χ set to 0 so that non-ionic interactions were ignored. Computing coacervate fraction with different temperatures as described below, we recorded an upper critical solution temperature (UCST) behavior, opposite to the trend of our observations (Fig S8). Counterion condensation suggests that for polyelectrolytes as highly charged as RNA, the effective charge density increases at higher temperature as determined below [24]. We suspect this increase in charge density due to counter ion release might favor CC formation at high temperature, accounting for its LCST behavior. We introduce counterion condensation in the FH-VO model refered to as the FH-VO-CR model. The FH-VO-CR model is able to captured the LCST behavior (Fig S9). However, without additinally introducing non-ionic interactions, the phase diagram computed by FH-VO-CR is still 1-2 orders of magnitude away from the range of experimental data. These results indicate that Voorn-Overbeek model without introducing non-ionic interactions are insufficient in describing tau-RNA CC.

In the FH-VO-CR model, we mimick the counterion condensation as a temperature dependent charge density for RNA, which is the only polymer species that is highly charge in our system, as

$$\sigma_q = \frac{l_q}{l_B} = \frac{4\pi\epsilon_0\epsilon_r k_B}{e^2} l_q T$$

Since the FH-VO-CR model is a rough approximation, for the purposes of qualitative investigation, here we constrained the size of amino acid l_p, nucleotide l_q, monovalent salt $l_{S+} = l_{S-} = l_S$ and water l_w to be 1.5×, 4.0×, 1× and 1× l_w, estimated from the lysozyme density, 0.70 mL/g [25], the DNA double helix width, 2 nm [26] and the ionic radii in aquous solution of Na^+ and Cl^- [27].

REFERENCE

[1] A. Pavlova, E. R. McCarney, D. W. Peterson, F. W. Dahlquist, J. Lew, and S. Han, "Site-specific dynamic nuclear polarization of hydration water as a generally applicable approach to monitor protein aggregation," *Phys. Chem. Chem. Phys. PCCP*, vol. 11, no. 31, pp. 6833–6839, Aug. 2009.

[2] D. W. Peterson, H. Zhou, F. W. Dahlquist, and J. Lew, "A soluble oligomer of tau associated with fiber formation analyzed by NMR," *Biochemistry (Mosc.)*, vol. 47, no. 28, pp. 7393–7404, Jul. 2008.

[3] A. Pavlova, C.-Y. Cheng, M. Kinnebrew, J. Lew, F. W. Dahlquist, and S. Han, "Protein structural and surface water rearrangement constitute major events in the earliest aggregation stages of tau," *Proc. Natl. Acad. Sci.*, vol. 113, no. 2, pp. E127–E136, 2016.

[4] S. Elbaum-Garfinkle *et al.*, "The disordered P granule protein LAF-1 drives phase separation into droplets with tunable viscosity and dynamics," *Proc. Natl. Acad. Sci. U. S. A.*, vol. 112, no. 23, pp. 7189–7194, Jun. 2015.

[5] A. Patel *et al.*, "A Liquid-to-Solid Phase Transition of the ALS Protein FUS Accelerated by Disease Mutation," *Cell*, vol. 162, no. 5, pp. 1066–1077, Aug. 2015.

[6] E. Hückel and P. Debye, "The theory of electrolytes: I. lowering of freezing point and related phenomena," *Phys Z*, vol. 24, pp. 185–206, 1923.

[7] J. Fu and J. B. Schlenoff, "Driving Forces for Oppositely Charged Polyion Association in Aqueous Solutions: Enthalpic, Entropic, but Not Electrostatic," *J. Am. Chem. Soc.*, vol. 138, no. 3, pp. 980–990, Jan. 2016.

[8] S. Kim *et al.*, "Complexation and coacervation of like-charged polyelectrolytes inspired by mussels," *Proc. Natl. Acad. Sci.*, vol. 113, no. 7, pp. E847–E853, Feb. 2016.

[9] A. S. Holehouse, K. Garai, N. Lyle, A. Vitalis, and R. V. Pappu, "Quantitative Assessments of the Distinct Contributions of Polypeptide Backbone Amides versus Side Chain Groups to Chain Expansion via Chemical Denaturation," *J. Am. Chem. Soc.*, vol. 137, no. 8, pp. 2984–2995, Mar. 2015.

[10] E. Spruijt, A. H. Westphal, J. W. Borst, M. A. Cohen Stuart, and J. van der Gucht, "Binodal Compositions of Polyelectrolyte Complexes," *Macromolecules*, vol. 43, no. 15, pp. 6476–6484, Aug. 2010.

[11] H.-K. Kwon, J. W. Zwanikken, K. R. Shull, and M. Olvera de la Cruz, "Theoretical Analysis of Multiple Phase Coexistence in Polyelectrolyte Blends," *Macromolecules*, vol. 48, no. 16, pp. 6008–6015, Aug. 2015.

[12] M. Rubinstein and R. H. Colby, *Polymer Physics*. OUP Oxford, 2003.

[13] M. Doi and S. F. Edwards, *The Theory of Polymer Dynamics*. Clarendon Press, 1988.

[14] K. T. Delaney and G. H. Fredrickson, “Recent Developments in Fully Fluctuating Field-Theoretic Simulations of Polymer Melts and Solutions,” *J. Phys. Chem. B*, vol. 120, no. 31, pp. 7615–7634, Aug. 2016.
[15] “Advanced Computational Field Theory Methods for Fluctuating Polymer Solutions - ProQuest.” [Online]. Available: https://search.proquest.com/openview/4c8b8e54782d4d6d5964834f0bdc88ec/1?pq-origsite=gscholar&cbl=18750&diss=y. [Accessed: 16-Jun-2018].
[16] G. Fredrickson, *The Equilibrium Theory of Inhomogeneous Polymers*. OUP Oxford, 2006.
[17] A. Alexander-Katz, A. G. Moreira, S. W. Sides, and G. H. Fredrickson, “Field-theoretic simulations of polymer solutions: Finite-size and discretization effects,” *J. Chem. Phys.*, vol. 122, no. 1, p. 014904, Dec. 2004.
[18] J. R. Klauder, “A Langevin approach to fermion and quantum spin correlation functions,” *J. Phys. Math. Gen.*, vol. 16, no. 10, p. L317, 1983.
[19] G. Parisi, “On complex probabilities,” *Phys. Lett. B*, vol. 131, no. 4, pp. 393–395, Nov. 1983.
[20] P. J. Flory and M. Volkenstein, “Statistical mechanics of chain molecules,” *Biopolymers*, vol. 8, no. 5, pp. 699–700.
[21] M. C. Villet and G. H. Fredrickson, “Efficient field-theoretic simulation of polymer solutions,” *J. Chem. Phys.*, vol. 141, no. 22, p. 224115, Dec. 2014.
[22] D. Düchs, K. T. Delaney, and G. H. Fredrickson, “A multi-species exchange model for fully fluctuating polymer field theory simulations,” *J. Chem. Phys.*, vol. 141, no. 17, p. 174103, Nov. 2014.
[23] K. T. Delaney and G. H. Fredrickson, “Theory of polyelectrolyte complexation—Complex coacervates are self-coacervates,” *J. Chem. Phys.*, vol. 146, no. 22, p. 224902, Jun. 2017.
[24] G. S. Manning, “Limiting Laws and Counterion Condensation in Polyelectrolyte Solutions I. Colligative Properties,” *J. Chem. Phys.*, vol. 51, no. 3, pp. 924–933, Aug. 1969.
[25] S. J. Perkins, “Protein volumes and hydration effects. The calculations of partial specific volumes, neutron scattering matchpoints and 280-nm absorption coefficients for proteins and glycoproteins from amino acid sequences,” *Eur. J. Biochem.*, vol. 157, no. 1, pp. 169–180, May 1986.
[26] G. M. Blackburn, *Nucleic Acids in Chemistry and Biology*. Royal Society of Chemistry, 2006.
[27] Y. Marcus, “Ionic radii in aqueous solutions,” *Chem. Rev.*, vol. 88, no. 8, pp. 1475–1498, Dec. 1988.

SI Figures

Figure S1

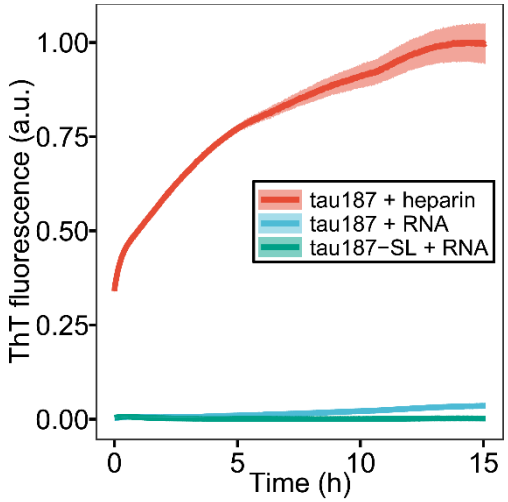

Figure S1 ThT fluorescence of tau-RNA CC. 100 μM of tau187 and tau187-SL was mixed with 300 μg/mL polyU RNA (RNA) at room temperature. 100 μM tau187 with 25 μM heparin was prepared as reference. Ribbon shows the standard deviation of 3 replicates.

FIGURE S2

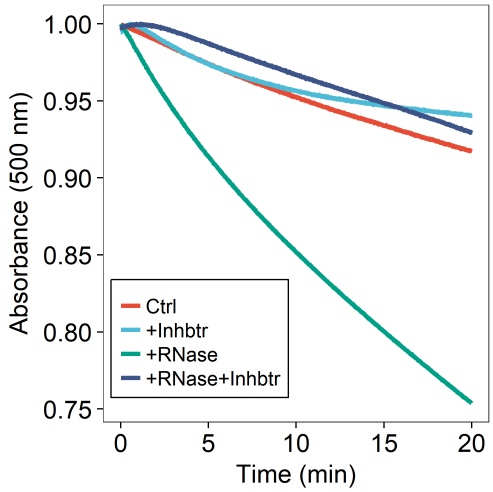

Figure S2 RNase induces turbidity decrease of tau187-RNA CC suspension. Tau187-RNA CCs were re-prepared with 100 μM tau187C291S and 300 μg/mL polyU RNA, while absorbance at 500 nm was monitored. Samples were treated with buffer (Ctrl), 1 U/μL RNase inhibitor (mainly inhibiting RNase A), 50 ng/mL RNase A, and 50 ng/mL RNase A with 1 U/μL RNase inhibitor.

FIGURE S3

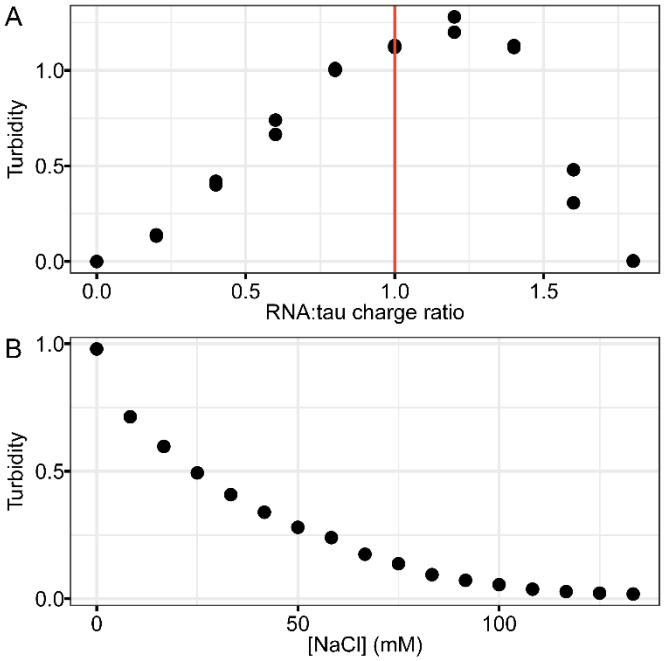

Figure S3 Turbidity of tau-RNA CC at varying charge ratios and ionic strength. (**A**) PolyU RNA was titrated into 20 μM tau187C291S in the buffer of 20 mM ammonium acetate at pH 7. Charge ratio was calculated based on the estimated charge for tau, +11 per tau molecule and the estimated charge for RNA, -1 per nucleotide. Turbidity was assigned from absorbance at λ = 500 nm. Red line indicates the place where the estimated RNA:tau charge ratio equals to 1. (**B**) 20 μM tau was mixed with 60 μg/mL RNA so that RNA:tau charge ratio equals to 1. NaCl was titrated into the mixture while turbidity was monitored.

FIGURE S4

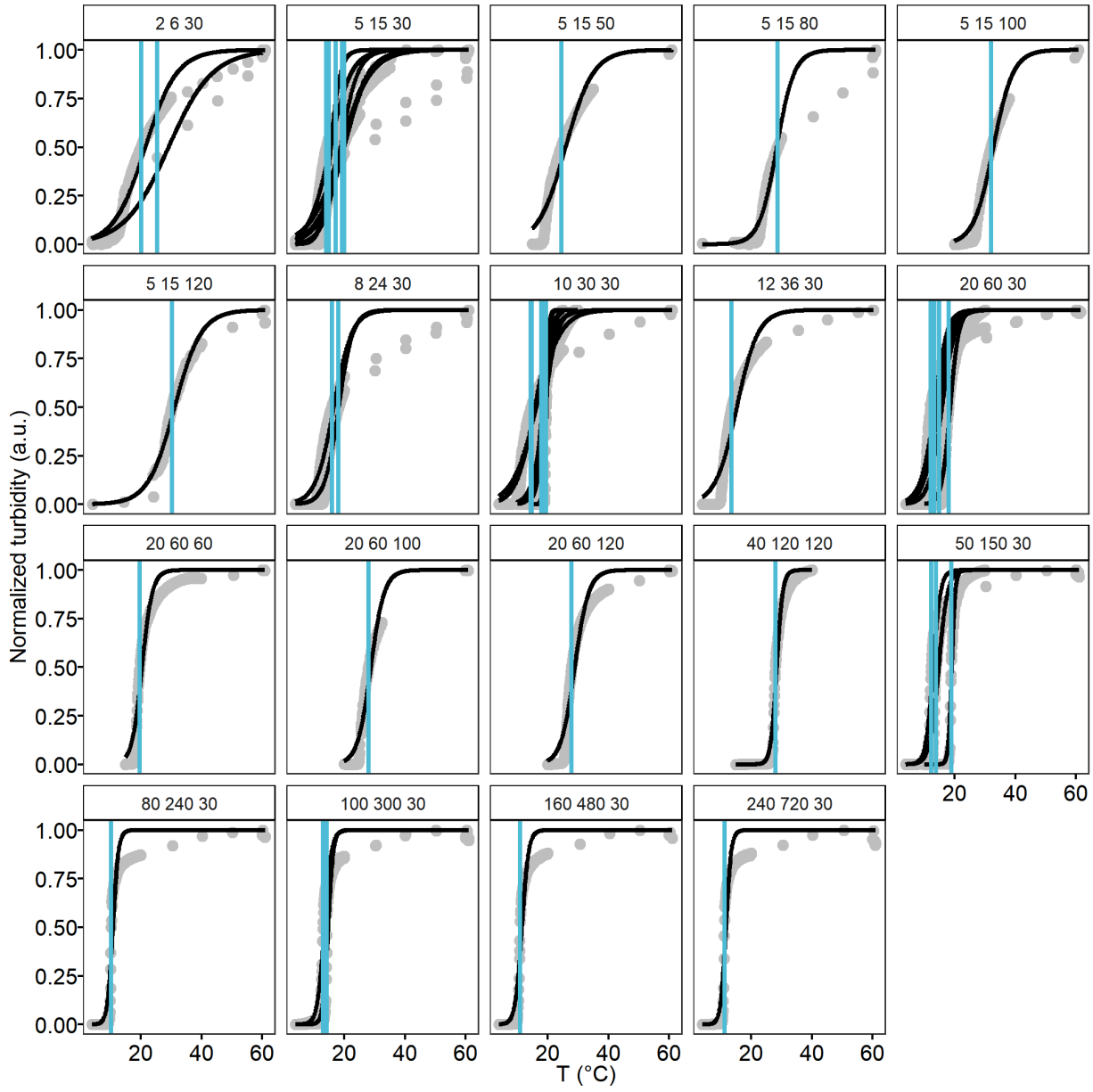

Figure S4 Turbidity-temperature data and cloud points determinations of various [tau] and [NaCl]. Tau187-RNA CCs were prepared at various concentration of [tau] and [NaCl] with fixed ratio of [RNA]:[tau], shown as strip text (e.g. "2 6 30" refers to [tau] = 2 μM, [RNA] = 6 μg/mL, [NaCl] = 30 mM). Samples were kept at 4 °C before ramping up temperature at 1 °C/min. Absorbance at 500 nm was monitored and used as turbidity (grey points). Turbidity-temperature data were fit to a sigmoid curve (black solid line), where the cloud point, T_{cp}, were determined (blue vertical line). [tau], [NaCl] and T_{cp} were used for theory and simulation modeling.

FIGURE S5

Tau114 vs Tau187

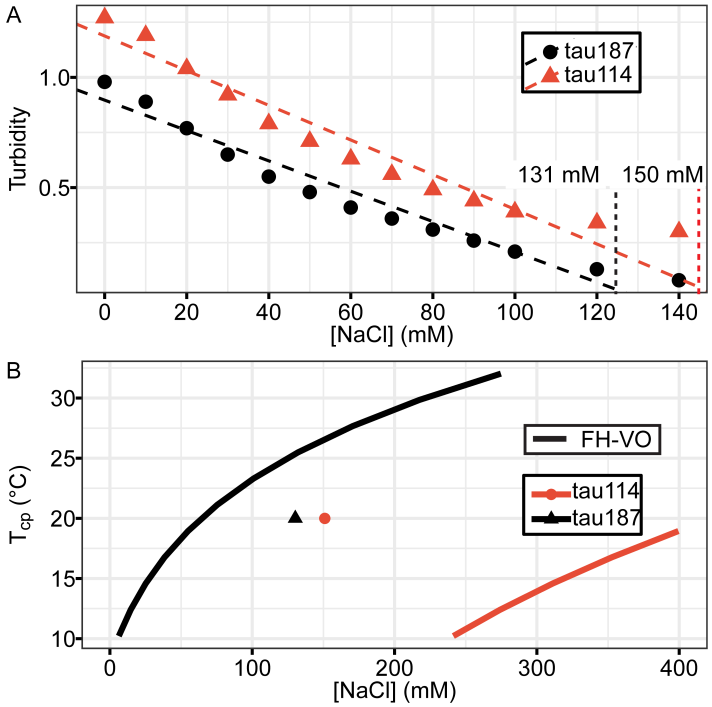

Figure S5 Phase diagrams of tau114 vs tau187. Tau-RNA CC were prepared with 20 μM tau187 with 60 μg/mL RNA (tau187) or 28 μM tau114 with 84 μg/mL RNA (tau114). **(A)** Turbidity was recorded with varying NaCl concentration. [NaCl] where turbidity vanished were determined by linear fitting to be 131 mM for tau187 and 150 mM for tau114. **(B)** [NaCl] vs. T_{cp} vs. [NaCl] curves for 20 μM tau187 or 28 μM tau114 were computed by FH-VO with $\chi = \chi(T_{cp})$ obtained from Figure 2D, shown together with the experimental data points obtained from (A).

FIGURE S6

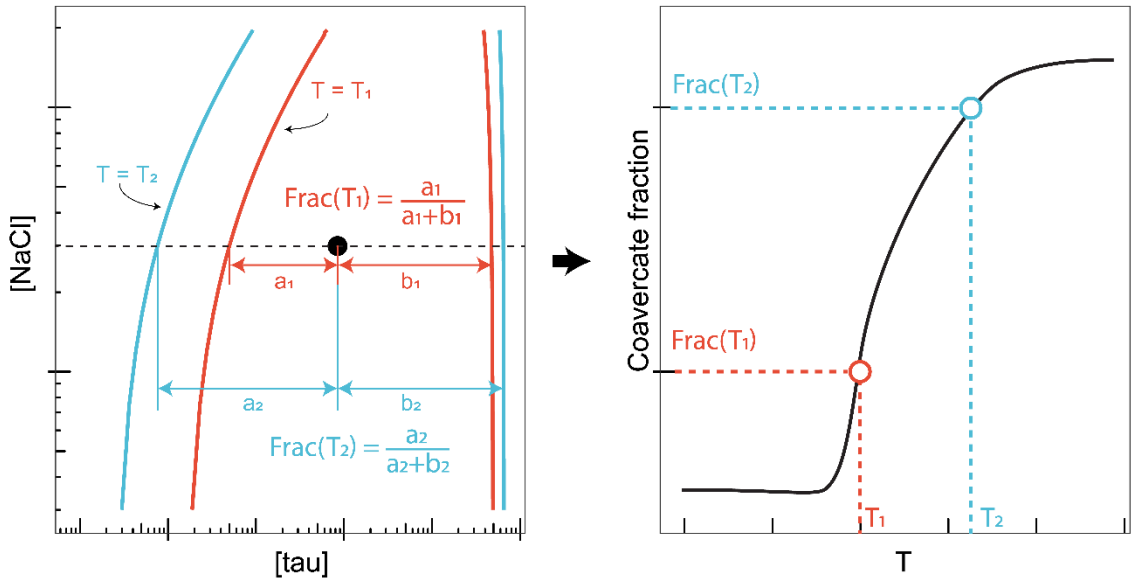

Figure S6 Schematic diagram of computing coacervate fraction from Binodal curves. Binodal curves were computed at different temperatures T_1, and T_2 (left panel). Given experimental conditions [tau] and [NaCl], the coacervate fraction (dense phase fraction) were calculated by the Lever rule. Multiple temperatures and calculated coacervate fractions were mapped to a curves showing, in this example, LCST behavior (right panel).

FIGURE S7

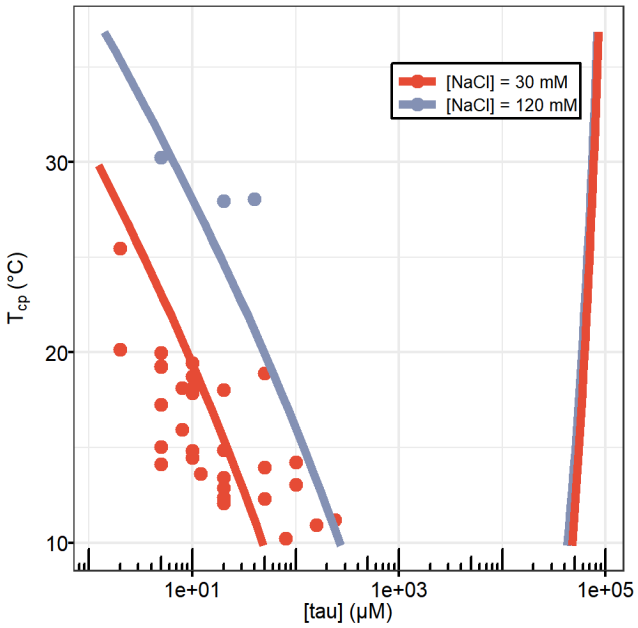

Figure S7 Full phase diagram of tau187-RNA CC. Experimental data showing [tau] vs Tcp was replot from Fig 2B (**points**). Binodal curves was generated by fitting the data to the FH-VO model (**solid lines**).

FIGURE S8

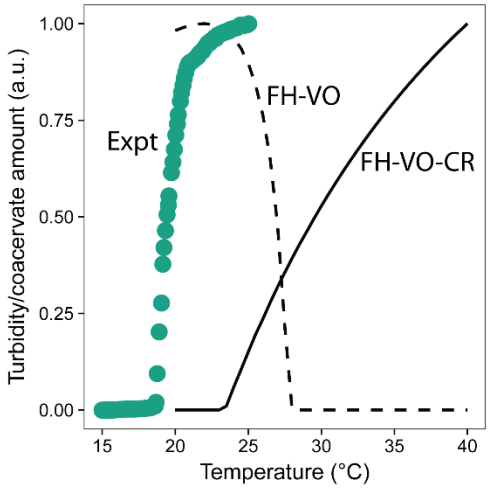

Figure S8 Coacervate amount of tau-RNA CC at different temperature. Experiment data were represented by absorbance at λ = 500 nm. Predicted coacervate fraction by FH-VO and FH-VO-CR models were computed at $(\boldsymbol{\phi_{polymer}}, \boldsymbol{\phi_{salt}}) = (\mathbf{0.01}, \mathbf{0.282})$ and $(\mathbf{0.006}, \mathbf{0.0216})$ respectively, which were chosen in order to capture the computed data within ranges of experimental temperatures. Coacervate fractions were normalized highlighting the trends.

FIGURE S9

FH-VO-CR finds LCST but missed quantitative accuracy

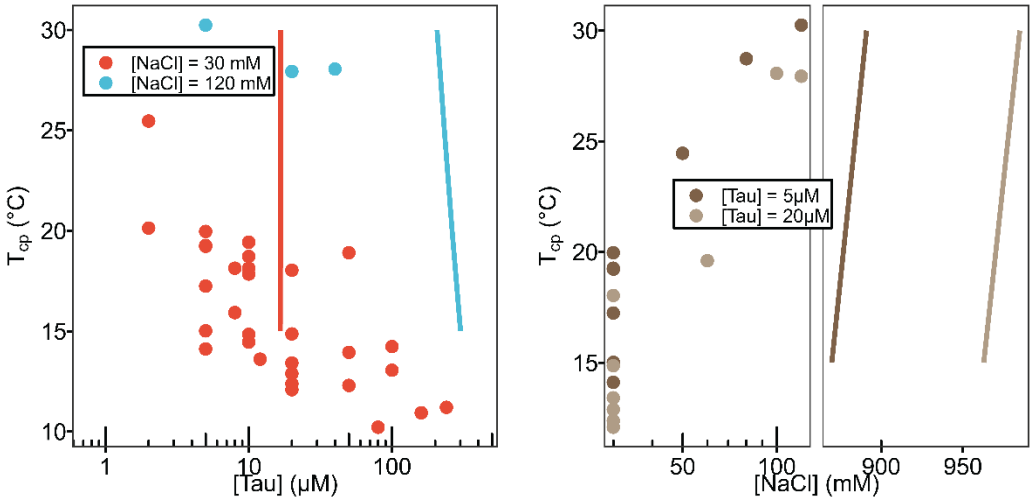

Figure S9 FH-VO-CR phase diagram of tau-RNA CC. Tau-RNA CC [Tau] vs. T_{cp} at different NaCl concentration (left panel), [NaCl] vs. T_{cp} at different tau concentrations (right panel) were re-plotted from Fig.2. Experimental data (solid points) were plotted against computed values (solid line).

FIGURE S10

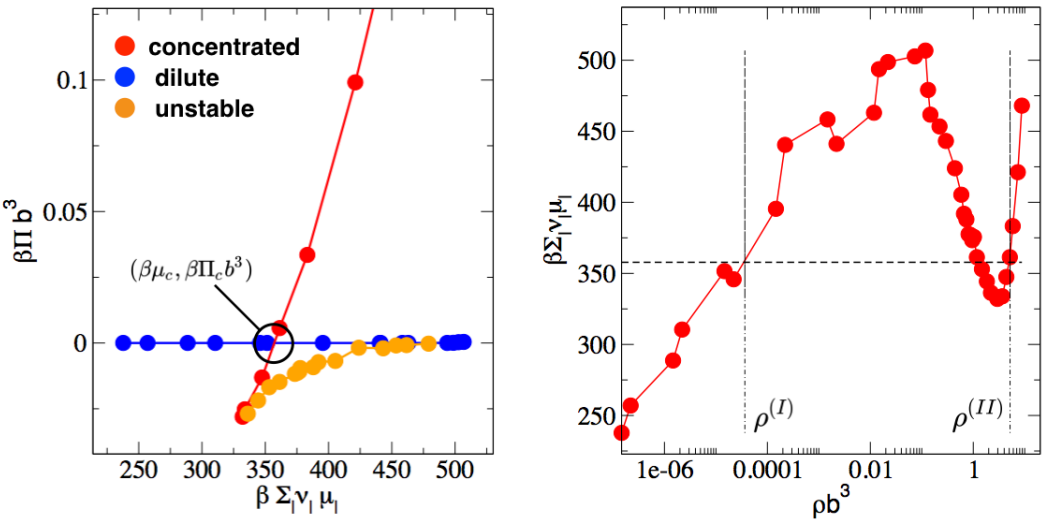

Figure S10 Determination of phase coexistence points from FTS. (Left). Parametric plot of FTS simulation data points of the osmotic pressure vs the chemical potential. The dilute phase is shown in blue and the concentrated phase (complex coacervate) is shown in red. The intersection point of the two branches is the condition for simultaneous equivalence of pressure and chemical potential for the two phases. (**Right**) The chemical potential vs. the total polymer density from FTS simulation (red points). The horizontal dashed line is the chemical potential at the phase coexistence point. Intersection of the data points with the horizontal dashed lines determines the supernatant (I) and complex-coacervate (II) coexisting polymer densities.

FIGURE S11

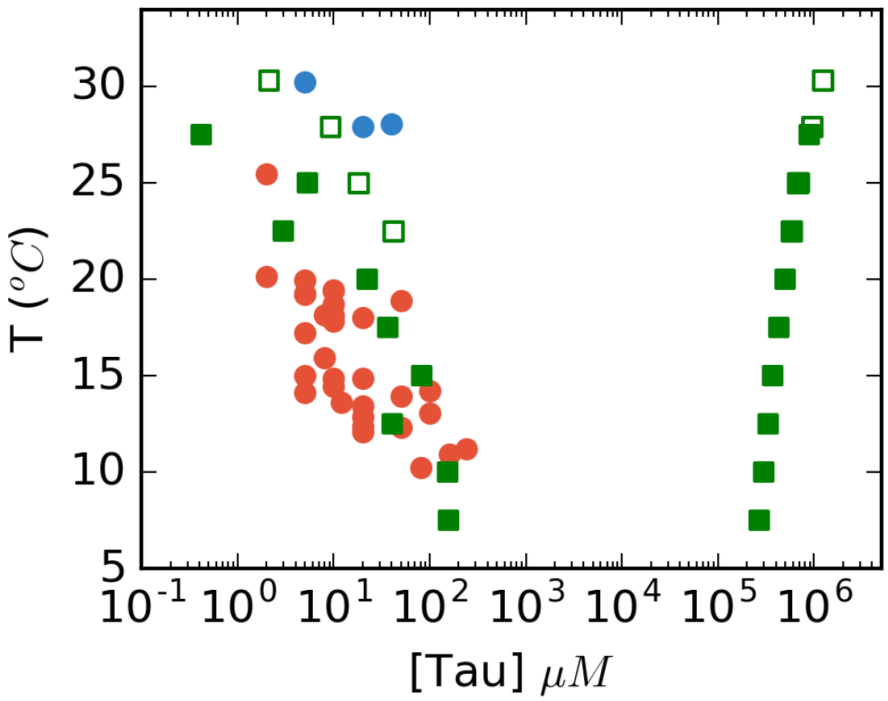

Figure S11 Full phase diagram of tau187-RNA CC from FTS. Low density points (left) are reproduced from Fig. 6 C in the main text. Filled green (low salt) and open green (120 mM NaCl) are obtain from FTS, and red and blue circles are corresponding experimental data. The right side of the figure shows the corresponding high density binodal curve predicted from FTS.

FIGURE S12

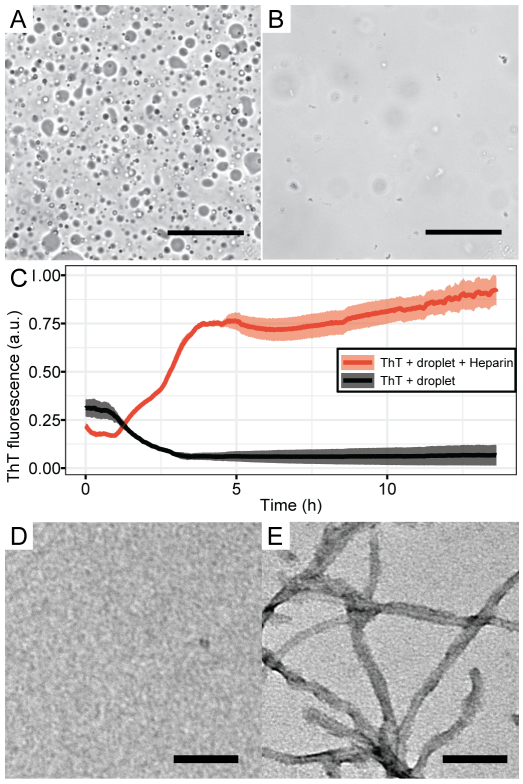

Figure S12 Tau-RNA CC upon addition of heparin. (**A**) 100 µM tau187C291S-SL and 300 µg/mL polyA RNA was mixed in the buffer of 20 mM ammonium acetate at pH 7, with 19 vol % glycerol. Images were taken after 10 minutes at room temperature. (**B**) Sample in A was re-prepared and incubated for 10 min. 25 µM heparin was added afterwards, immediately followed by imaging. The scale bars in both A and B are 50 µm long. **(C)** ThT fluorescences of samples in A and B were monitored with additional 10 µM ThT. **(D)** TEM images of sample in A after overnight incubation, showing no structures similar to amyloid fibrils. **(E)** TEM images of sample in B after overnight incubation, showing structures with length and width consistent with tau fibrils. The scale bars in both D and E are 200 nm long.

TABLE S1

tau	sequence	length
tau187	MGSSH HHHHH SSGLV PRGSH MVKSK IGSTE NLKHQ PGGGK VQIIN KKLDL SNVQS KSGSK DNIKH VPGGG SVQIV YKPVD LSKVT SKCGS LGNIH HKPGG GQVEV KSEKL DFKDR VQSKI GSLDN ITHVP GGGNK KIETH KLTFR ENAKA KTDHG AEIVY KSPVV SGDTS PRHLS NVSST GSIDM VDSPQ LATLA DEVSA SLAKQ GL	207
tau114	MGSSH HHHHH SSGLV PRGSH MVKSK IGSTE NLKHQ PGGGK VQIIN KKLDL SNVQS KSGSK DNIKH VPGGG SVQIV YKPVD LSKVT SKCGS LGNIH HKPGG GQVEV KSEKL DFKDR VQSKI GSLDN ITHVP GGGN	134

Table S1 Primary sequences of tau187 and tau114 used in the experiments and VO-FH calculation.

TABLE S2

species	N	net charge	σ
tau187	207	+11.0	+0.053
tau114	134	+10.7	+0.075
RNA	2939	−2939	−1
Na+	1	+1	+1
Cl−	1	−1	−1
water	1	0	0

Table S2 Degree of polymerization and average charge densities of species used in the VO-FH calculation. N, degree of polymerization; net charge, estimated net charge per molecule; σ, average charge per monomer.

TABLE S3

T (K)	α	VO-FH		FTS	
		ϵ_H/T	ϵ_S	ϵ_H/T	ϵ_S
300	3.97	-1.3	1.8	-0.370	0.876

total salt (mM)	$\phi_{tau} + \phi_{RNA}$	ϕ_{water}	ΔH_{D-H} (kJ • mol^{-1}) per lattice site	ΔH (kJ • mol^{-1}) per tau monomer	$T\Delta S$ (kJ • mol^{-1}) per tau monomer
50	0.283	0.716	-0.050	-2.321	-3.214
100	0.277	0.722	-0.051	-2.339	-3.239
150	0.271	0.727	-0.051	-2.356	-3.262
200	0.265	0.732	-0.052	-2.372	-3.284

Table S3 Thermodynamics calculated by VO-FH at 300 K and physiological relevant salt concentrations. T = 300 K was used to determine α, ε_H/T and ε_S. At this temperature, 50 mM ~ 200 mM total salt concentration was used to calculated binodal compositions as described in SI Methods. The calculated composition of tau, RNA and water in the dense phase was listed as $\phi_{tau}+ \phi_{RNA}$ and ϕ_{water}. ΔH_{D-H}, the Debye-Huckel approximated phase separation enthalpy; ΔH, the Flory-Huggins phase separation enthalpy and $T\Delta S$, the Flory-Huggins phase separation entropy.